Dynamic Transmission Error Prediction of Helical Gear Pair Under Sliding Friction Using Floquet Theory

Song He
e-mail: he.81@osu.edu

Rajendra Singh
Fellow ASME
e-mail: singh.3@osu.edu

Acoustics and Dynamics Laboratory,
Department of Mechanical Engineering,
The Ohio State University,
Columbus, OH 43210

An analytical solution to the dynamic transmission error of a helical gear pair is developed by using a single-degree-of-freedom model with piecewise stiffness functions that characterize the contact plane dynamics and capture the velocity reversal at the pitch line. By assuming a constant mesh stiffness density along the contact lines, a linear time-varying model (with parametric excitations) is obtained, where the effect of sliding friction is quantified by an effective mesh stiffness term. The Floquet theory is then used to obtain closed-form solutions to the dynamic transmission error, and responses are derived to both initial conditions and the forced periodic function under a nominal preload. Analytical models are validated by comparing predictions with numerical simulations, and the effect of viscous damping is examined. Stability analysis is also briefly conducted by using the state transition matrix. Overall, the sliding friction has a marginal effect on the dynamic transmission error of helical gears, as compared with spur gears, in the context of the torsional model. [DOI: 10.1115/1.2890115]

1 Introduction

This paper is an extension of our recent work [1] in which we proposed a 12-degree-of-freedom (DOF), linear time-varying (LTV) analytical model for helical gears that characterizes the contact plane dynamics and captures the velocity reversal at the pitch line due to sliding friction. Earlier, Velex and Cahouet [2] found that the dynamic bearing forces (as related to the sliding friction in helical or spur gears) can indeed generate significant time-varying excitations at lower speeds. Velex and Sainsot [3] examined friction excitations in errorless spur and helical gear pairs and reported that the friction appears as a non-negligible excitation source, especially for translating motions. Lundvall et al. [4] proposed a multibody model for spur gears and briefly discussed the role of profile modification in the presence of sliding friction. Vaishya and Singh [5–7] illustrated frictional issues for spur gears by assuming equal load sharing among the contact teeth. This assumption leads to a rectangular variation in mesh stiffness, which is a special case (zero helical angle) of a generic trapezoidal stiffness profile for helical gears. To overcome this deficiency [5–7], we have developed a more accurate model of the spur gears that incorporates realistic mesh stiffness and sliding friction [8]. Many of the models cited above are solved numerically. Thus, there is a clear need for analytical (closed form) solutions to the dynamic response of a helical gear pair under the influence of sliding friction. In fact, Vaishya and Singh [6] applied the Floquet theory to a simplified spur gear model to predict responses of parametrically excited system and to assess the system stability. Our paper will enhance Vaishya and Singh's work [6] by applying the Floquet theory to a helical gear pair.

2 Linear Time-Varying Formulation

The chief objectives of this paper are as follows. First is to place emphasis on periodic frictional effects at the gear tooth interface by ignoring other directional properties and the auxiliary components of the gearbox [1]. This will allow us to describe the single mesh helical geared system as a simplified single-degree-of-freedom (SDOF), LTV oscillator with piecewise linear effective mesh stiffness; frictional forces/moments will be formulated as parametric excitations. Second is to derive closed-form solutions for the LTV system in terms of the dynamic transmission error (DTE) under both homogeneous and forced conditions by using the Floquet theory. Third is to validate the proposed theory by using the numerical integration method. Key assumptions include the following: (1) The vibratory motions are small compared with the kinematical motion, so that the position of the contact lines and the relative sliding velocity depend only on the mean angular motions of the gear pair. (2) The mesh stiffness per unit length along the contact lines (i.e., stiffness density k) is constant [1]; this is equivalent to the equal load sharing assumption in spur gears [5–7]. (3) Coulomb's law with a constant coefficient of friction (μ) is employed [1–8] though mixed lubrication regimes exist [9]. (4) The bearing stiffness is assumed to be much higher than the mesh stiffness, and thus the shaft/bearings could be simplified as rigid connections. Hence, only the torsional DOFs are considered in terms of DTE. Also, it is assumed that the mean load is high such that the dynamic load is insufficient to cause any tooth separations [10,11].

The helical geared system is depicted in Fig. 1, where the pinion and gear are modeled as rigid cylinders linked by a series of independent stiffness elements that describe the contact plane tangent to the base cylinders [1]. The pinion and gear dynamics are formulated in the coordinate systems located at their respective centers; the nominal motions are given as $-\Omega_p e_z$ and $\Omega_g e_z = e_z \Omega_p r_{bp}/r_{bg}$. Here, the z axis coincides with the axial direction, e is the unit directional vector, and r_{bp} and r_{bg} are the base radii of pinion and gear. An (static) input torque T_p is applied to the pinion, and the (static) braking torque T_g on the gear obeys the basic gear kinematics. Superimposed on the kinematic motions are rotational vibratory motions denoted by θ_{zp} and θ_{zg} for the pinion and gear. Analytical formulations are demonstrated via the following sample case with parameters of the pinion (relevant gear parameters are within the parentheses): number of teeth, 25 (31); outside diameter, 3.38 (4.13) in.; pitch diameter, 3.125 (3.875) in.; root diameter, 2.811 (3.56) in.; center distance,

Contributed by the Power Transmission and Gearing Committee of ASME for publication in the JOURNAL OF MECHANICAL DESIGN. Manuscript received May 6, 2007; final manuscript received August 17, 2007; published online April 1, 2008. Review conducted by Avinash Singh.

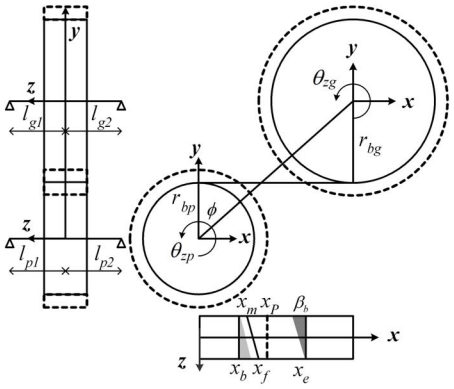

Fig. 1 Schematic of the helical gear pair system

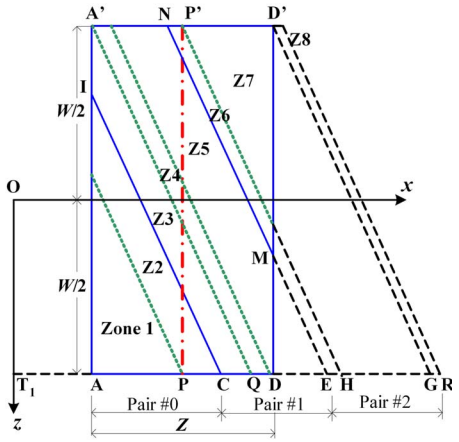

Fig. 2 Contact zones at the beginning of a mesh cycle within the contact plane. Key: *PP′* is the pitch line; *AA′* is the face width *W*; *AD* is the length of contact zone *Z*.

3.5 in.; transverse diametral pitch, 8 in.^{-1}; transverse pressure angle, 25 deg, helix angle, $\beta_b=21.5$ deg, face width, $W=1.25$ in.; polar moment of inertia, $J_{pz}=8.33\times10^{-3}$ ($J_{gz}=1.64\times10^{-2}$) lb s^2 in.; and mass, 1.26×10^{-2} (1.58×10^{-2}) lb $\text{s}^2/\text{in.}^{-1}$. Since the overall contact ratio $\sigma_c=2.7$, either two or three tooth pairs are in contact at any time instant. The three meshing tooth pairs within one mesh cycle are numbered as 0, 1, and 2, respectively. A constant mesh stiffness density (k) along the contact lines could be estimated via a static analysis by using the finite element/contact mechanics (FE/CM) formulation [12,13].

A simplified SDOF model could be derived in items of DTE $\delta(t)=r_{bp}\theta_{zp}(t)+r_{bg}\theta_{zg}(t)$ at the gear mesh by assuming rigid links at the shaft/bearings. Note that the dynamic mesh forces oriented in other directions (such as the sliding force in the off line-of-action (OLOA) direction) still need to be formulated [1] for calculations of the dynamic moments in the torsional direction. Hence, the effective torsional stiffness should have contributions from both the sliding friction and the time-varying elastic tooth stiffness due to the Hertzian contact.

For multiple tooth pairs in contact, $n=\text{ceil}(\sigma_c)$ ($n=3$ for the sample case) pairs of meshing teeth need to be formulated, where the "ceil" function rounds σ_c to the nearest integers toward infinity. Figure 2 illustrates the snapshot at the beginning of a mesh cycle. At this instant, pair 0 (defined as $x_0(t)=\text{mod}(\Omega_p r_{bp}t,\lambda)+L_{T_1A}$, where λ is the base pitch, L represents the geometrical distance, the modulus function is $\text{mod}(x,y)=x-y\cdot\text{floor}(x/y)$ for $y\neq0$, and the "floor" function rounds x/y to the nearest integer toward minus infinity) just comes into mesh at point A and pair 1 (defined as $x_1(t)=\text{mod}(\Omega_p r_{bp}t,\lambda)+\lambda+L_{T_1A}$) is in contact along line CI. Likewise, pair 2 (defined as $x_2(t)=\text{mod}(\Omega_p r_{bp}t,\lambda)+2\lambda+L_{T_1A}$) contacts each other along line MN. As the gears roll, the contact lines move diagonally across the contact zone. When pair 0 reaches pitch point P, the relative sliding velocity between pinion and gear starts to reverse, resulting in a reversal of friction force along the portion of contact line beyond the pitch point. Once pair 0 reaches line CI (and pair 1 reaches line MN) in the end of the mesh circle, pair 0 becomes pair 1 (and pair 1 becomes pair 2), corresponding to the start of the next mesh cycle. The dynamic tooth stiffness functions $K_{p,i}(t)$ and $K_{g,i}(t)$ are defined below where $M_{p,i}(t)$ and $M_{g,i}(t)$ are the dynamic moments on the pinion and gears, respectively [1],

$$K_{p,i}(t)=\frac{M_{p,i}(t)}{r_{bp}\delta(t)} \tag{1a}$$

$$K_{g,i}(t)=\frac{M_{g,i}(t)}{r_{bg}\delta(t)} \quad (i=0,1,2) \tag{1b}$$

For the sample case, $K_{p,i}(t)$ and $K_{g,i}(t)$ are explicitly derived for each meshing tooth pair over eight contact zones (Zi), as shown in Fig. 2. Also, refer to Ref. [1] for details. Zones 1 and 2 correspond to pair 0 before and after reaching the pitch line; Zones 3–5 and Zones 6–8 correspond to pairs 1 and 2, respectively. The stiffness values of the two contact zones for the first pair (0) are derived as follows, where x_m, x_f, z_m, and z_f denote the lower and upper limits [1] along x and z axes, as shown in Fig. 1,

$$K_{p,0}(t)=\begin{cases}\dfrac{k}{r_{bp}}\left[-\dfrac{\mu}{2}(x_f(t)+x_m)+r_{bp}\cos\beta_b\right](z_f-z_m(t)) & \text{(Z1)}\\ \dfrac{k}{r_{bp}}\left[-\dfrac{\mu}{2}(x_p+x_m)(z_p(t)-z_m(t))+r_{bp}\cos\beta_b(z_f-z_m(t))+\dfrac{\mu}{2}(x_f(t)+x_p)(z_f-z_p(t))\right] & \text{(Z2)}\end{cases} \tag{2a}$$

$$K_{g,0}(t)=\begin{cases}\dfrac{k}{r_{bg}}\left[\dfrac{\mu}{2}(x_f(t)+x_m-2x_g)+r_{bg}\cos\beta_b\right](z_f-z_m(t)) & \text{(Z1)}\\ \dfrac{k}{r_{bg}}\left[\dfrac{\mu}{2}(x_p+x_m)(z_p-z_m(t))-\dfrac{\mu}{2}(x_f(t)+x_p)(z_f-z_p(t))+x_g\mu(z_f+z_m(t)-2z_p(t))+r_{bg}\cos\beta_b(z_f-z_m(t))\right] & \text{(Z2)}\end{cases} \tag{2b}$$

The second meshing tooth pair (1) is classified into Zones 3–5, as shown in Fig. 2. Its composite torsional stiffness could be derived for the pinion and gear as

$$K_{p,1}(t)=\begin{cases}\dfrac{k}{r_{bp}}\left[-\dfrac{\mu}{2}(x_p+x_m)(z_p(t)-z_m(t))+\dfrac{\mu}{2}(x_f(t)+x_p)(z_f-z_p(t))+r_{bp}\cos\beta_b(z_f-z_m(t))\right] & \text{(Z3)}\\ \dfrac{k}{r_{bp}}\left[-\dfrac{\mu}{2}(x_p+x_m(t))(z_p(t)-z_m)+\dfrac{\mu}{2}(x_f(t)+x_p)(z_f-z_p(t))+r_{bp}\cos\beta_b(z_f-z_m(t))\right] & \text{(Z4)}\\ \dfrac{k}{r_{bp}}\left[-\dfrac{\mu}{2}(x_p+x_m(t))(z_p(t)-z_m)+\dfrac{\mu}{2}(x_f+x_p)(z_f(t)-z_p(t))+r_{bp}\cos\beta_b(z_f(t)-z_m)\right] & \text{(Z5)}\end{cases} \tag{3a}$$

$$K_{g,1}(t)=\begin{cases}\dfrac{k}{r_{bg}}\left[\dfrac{\mu}{2}(x_p+x_m)(z_p(t)-z_m(t))-\dfrac{\mu}{2}(x_f(t)+x_p)(z_f-z_p(t))+x_g\mu(z_f+z_m(t)-2z_p(t))+r_{bg}\cos\beta_b(z_f-z_m(t))\right] & \text{(Z3)}\\ \dfrac{k}{r_{bg}}\left[\dfrac{\mu}{2}(x_p+x_m(t))(z_p(t)-z_m)-\dfrac{\mu}{2}(x_f(t)+x_p)(z_f-z_p(t))+x_g\mu(z_f+z_m-2z_p(t))+r_{bg}\cos\beta_b(z_f-z_m)\right] & \text{(Z4)}\\ \dfrac{k}{r_{bg}}\left[\dfrac{\mu}{2}(x_p+x_m(t))(z_p(t)-z_m)-\dfrac{\mu}{2}(x_f+x_p)(z_f(t)-z_p(t))+x_g\mu(z_f(t)+z_m-2z_p(t))+r_{bg}\cos\beta_b(z_f(t)-z_m)\right] & \text{(Z5)}\end{cases} \tag{3b}$$

The third meshing tooth pair (2) is divided into zones 6–8, as shown in Fig. 2. Its composite torsional stiffness could be derived for the pinion and gear as

$$K_{p,2}(t)=\begin{cases}\dfrac{k}{r_{bp}}\left[-\dfrac{\mu}{2}(x_p+x_m(t))(z_p(t)-z_m)+\dfrac{\mu}{2}(x_f+x_p)(z_f(t)-z_p(t))+r_{bp}\cos\beta_b(z_f(t)-z_m)\right] & \text{(Z6)}\\ \dfrac{k}{r_{bp}}\left[\dfrac{\mu}{2}(x_f+x_m(t))+r_{bp}\cos\beta_b\right](z_f(t)-z_m) & \text{(Z7)}\\ 0 & \text{(Z8)}\end{cases} \tag{4a}$$

$$K_{g,2}(t)=\begin{cases}\dfrac{k}{r_{bg}}\left[\dfrac{\mu}{2}(x_p+x_m(t))(z_p(t)-z_m)-\dfrac{\mu}{2}(x_f+x_p)(z_f(t)-z_p(t))+x_g\mu(z_f(t)+z_m-2z_p(t))+r_{bg}\cos\beta_b(z_f(t)-z_m)\right] & \text{(Z6)}\\ \dfrac{k}{r_{bg}}\left[\dfrac{\mu}{2}(x_f+x_m(t))+r_{bp}\cos\beta_b\right](z_f(t)-z_m) & \text{(Z7)}\\ 0 & \text{(Z8)}\end{cases} \tag{4b}$$

The undamped torsional equations for the pinion and gear are derived as follows:

$$J_{pz}\ddot{\theta}_{zp}(t)+\sum_{i=0}^{2}r_{bp}K_{p,i}(t)[\delta(t)-\varepsilon(t)]=T_p \tag{5}$$

$$J_{gz}\ddot{\theta}_{zg}(t)+\sum_{i=0}^{2}r_{bg}K_{g,i}(t)\delta(t)=-T_g \tag{6}$$

We define DTE $\delta(t)$ and reduce Eqs. (5) and (6) into one equation, which describes an equivalent translational definite system as follows, where $\varepsilon(t)$ is the unloaded static transmission error. A time-varying viscous damping coefficient $C_e(t)$ is also included given (assumed) damping ratio ζ_e,

$$m_e\ddot{\delta}(t)+C_e(t)[\dot{\delta}(t)-\dot{\varepsilon}(t)]+K_e(t)[\delta(t)-\varepsilon(t)]=F_e \tag{7a}$$

$$m_e=\frac{J_{pz}J_{gz}}{r_{bg}^2J_{pz}+r_{bp}^2J_{gz}} \tag{7b}$$

$$K_e(t)=\sum_{i=0}^{2}K_{e,i}(t)=\sum_{i=0}^{2}\frac{r_{bp}^2J_{gz}K_{p,i}(t)+r_{bg}^2J_{pz}K_{g,i}(t)}{r_{bg}^2J_{pz}+r_{bp}^2J_{gz}} \tag{7c}$$

$$C_{e,i}(t)=2\zeta_e\sqrt{m_eK_e(t)} \tag{7d}$$

$$F_e=\frac{r_{bp}T_pJ_{gz}-r_{bg}T_gJ_{pz}}{r_{bg}^2J_{pz}+r_{bp}^2J_{gz}} \tag{7e}$$

Here, m_e is the effective mass defined in the torsional-transverse direction and F_e is the effective external force due to the nominal torques applied at the pinion and gear. The periodic effective stiffness function $K_{e,i}(t)$ of the ith meshing mesh pair is piecewise linear, and it incorporates contributions from both the mesh tooth stiffness and the sliding friction. The frictional influence on $K_{e,i}(t)$ is illustrated in Fig. 3 over eight contact zones, where a generic effective stiffness function is obtained by following a single tooth pair for three complete mesh cycles since ceil$(\sigma_c)=3$. When $\mu=0$ (no friction), $K_{e,i}(t)$ has a symmetric trapezoidal profile; when high sliding friction is introduced with $\mu=0.4$, additional discontinuities in the slope emerge during the transitions from Zone 1 to Zone 2, as well as from Zone 6 to Zone 7. These correspond to the conditions when the contact line reaches or leaves the pitch line. Note that the stiffness functions are "continuous" in a piecewise manner due to the gradual approaching and recess motions of the helical gear pair. Compared with the square-wave-shaped tooth stiffness function of a spur gear pair [5–8], this shape should be more favorable as lower vibroacoustic levels would be expected.

Given the piecewise stiffness $K_e(t)$ of Eqs. (7*a*)–(7*e*), we denote j as the index for the jth interval (with a constant slope) and define the generic periodic stiffness function $K_{e,j}(t)$ over m piecewise intervals within one mesh cycle as follows:

$$K_{e,j}(t)=K_{e,j}(t+T)=K_{e,j-1}+\frac{K_{e,j}-K_{e,j-1}}{t_j-t_{j-1}}(t-t_{j-1}) \tag{8}$$

For the sample case with individual $K_{e,i}(t)$ $(i=0,\ldots,2)$ of Fig. 3, the combined stiffness functions $K_{e,j}(t)$ $(j=1,\ldots,6)$ are calculated over six contact regions within one mesh cycle. Since the slope is constant within each region, only the stiffness values $K_{e,j}$ at the

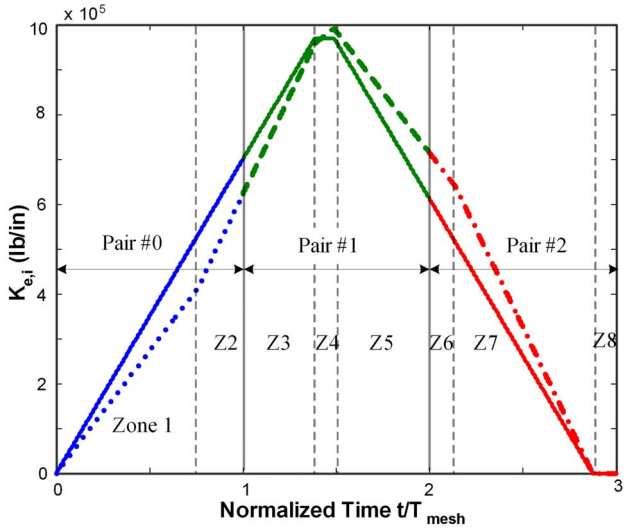

Fig. 3 Individual effective stiffness $K_{e,i}(t)$ along the contact zone, where T_{mesh} is one mesh cycle. Key: blue solid line, tooth pair 0 (μ=0); green solid line, tooth pair 1 (μ=0); red solid line, tooth pair 2 (μ=0); blue dotted line, tooth pair 0 (μ=0.4);green dashed line, tooth pair 1 (μ=0.4); and red dashed-dotted line, tooth pair 2 (μ=0.4).

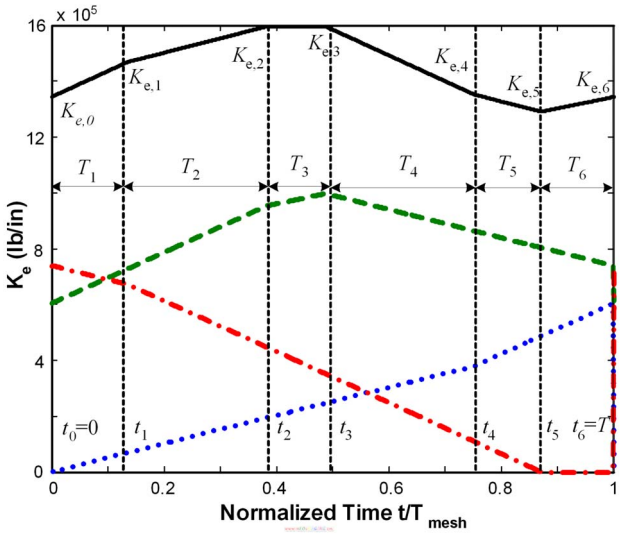

Fig. 4 Piecewise effective stiffness function defined in six regions within one mesh cycle withμ=0.4. Key: blue dotted line, tooth pair 0; green dashed line, tooth pair 1; red dashed-dotted line, tooth pair 2; and black solid line, combined stiffness function.

starting and ending time instants are needed with $K_{e,6}=K_{e,0}$ due to the periodicity. The time instants t_i of each region within one period could be determined based on Fig. 2 as follows: $t_0=0$, $t_1=(L_{EH}/\lambda)T$, $t_2=(L_{CQ}/\lambda)T$, $t_3=(L_{CD}/\lambda)T$, $t_4=(L_{AP}/\lambda)T$, $t_5=(L_{EG}/\lambda)T$, and $t_6=T$. Table 1 lists the relationship between the six contact regions defined for the combined stiffness functions $K_{e,j}(t)$ and the eight contact zones defined for individual meshing tooth pairs as given by $K_{e,i}(t)$. Although the number of contact zones/regions depends on the gear geometry, the proposed modeling strategy could be easily applied to other helical geared systems.

Figure 4 compares the combined $K_{e,j}(t)$ and individual $K_{e,i}(t)$ functions over one period. Observe that the profile of $K_{e,j}(t)$ resembles those of individual $K_{e,i}(t)$: Under zero friction, $K_{e,j}(t)$ follows a symmetric trapezoidal pattern, where four piecewise intervals exist within one mesh cycle. When the sliding friction is included, two additional discontinuities in the slope are introduced at the transitions from Region 1 to Region 2, as well as from Region 4 to Region 5. Hence, six piecewise regions need to be analyzed for one complete mesh cycle. Note that a high mean component exists for the combined $K_{e,j}(t)$, whose values are always positive (nonzero).

Table 1 Relationship between contact zones and contact regions for the NASA-ART helical gear pair

Contact region	Contact zones of Fig. 2		
	Pair 0	Pair 1	Pair 2
1	Z1	Z3	Z6
2	Z1	Z3	Z7
3	Z1	Z4	Z7
4	Z1	Z5	Z7
5	Z2	Z5	Z7
6	Z2	Z5	Z8

3 Analytical Solutions by the Floquet Theory

Vaishya and Singh [6] suggested analytical solutions to a SDOF spur gear system model with periodic square-wave stiffness. For a helical gear pair, $K_{e,i}(t)$ varies periodically in a trapezoidal pattern; hence, the spur gear could be treated as a special (limiting) case of the helical gear model [14,15] where the slope of stiffness within each interval is zero rather than an arbitrary constant. Assuming that $\varepsilon(t)=0$ (perfect involute profile) and $C_e(t)=0$ (undamped condition), the parametrically excited system of Eqs. (7*a*)–(7*e*) under a mean load F_e is simplified as follows:

$$m_e\ddot{\delta}(t)+K_e(t)\delta(t)=F_e \tag{9}$$

The Floquet theory [16] is then applied to find analytical solutions to both free (including the case with a viscous damping $C_e=2\zeta_e\sqrt{m_eK_e}$) and forced responses. For the sample case, six contact regions need to be formulated with the influence of sliding friction. Rewrite the governing equation in the state space form as

$$\dot{X}(t)=G(t)X(t)+F(t) \tag{10a}$$

$$G(t+T)=G(t) \tag{10b}$$

$$G(t)=\begin{cases} G_1(t), & 0\leqslant t<t_1 \\ G_j(t), & t_{j-1}\leqslant t<t_j \quad (i=2,\ldots,5) \\ G_6(t), & t_5\leqslant t<T \end{cases} \tag{10c}$$

$$X(t)=\begin{Bmatrix} \delta(t) \\ \dot{\delta}(t) \end{Bmatrix} \tag{10d}$$

$$F(t)=\begin{Bmatrix} 0 \\ F_e/m_e \end{Bmatrix} \tag{10e}$$

The solution over one complete mesh cycle T is written in the form of a state transition matrix (Φ). For a piecewise periodic system, this matrix may further be decomposed into Φ_j over each contact region [6] in Eq. (11), where the functions are continuously differentiable and analytical solutions to the homogeneous equation exist,

$$\Phi(T,0) = \Phi(T,t_5) \cdot \cdot \cdot \Phi(t_2,t_1)\Phi(t_1,0) \tag{11}$$

Each $\Phi(t_j,t_{j-1})$ is evaluated from the Wronskian matrix (Π) as

$$\Phi(t_j,t_{j-1}) = \Pi(t_j)\Pi^{-1}(t_{j-1}), \quad t_{j-1} \leqslant t \leqslant t_j \tag{12a}$$

$$\Pi(t) = \begin{bmatrix} \gamma_1 & \gamma_2 \\ \dot{\gamma}_1 & \dot{\gamma}_2 \end{bmatrix} \tag{12b}$$

Here, γ_1 and γ_2 are two basis solutions to the homogeneous equation $\dot{X}(t)=G(t)X(t)$. By using the periodic property of Φ, the Floquet theory extends solutions to future states of the system that are apart by n mesh cycles. Thus, the state transition matrix $\Phi(nT,0)$ over n cycles and the resulting responses $X(t)$ are given by

$$\Phi(nT,0) = \Phi(T,0)^n \tag{13}$$

$$X(t) = \Phi(t,0)X(0) + \int_0^t \Phi(t,\tau)F(\tau)d\tau \tag{14a}$$

$$X(t+nT) = \Phi^n(T,0)X(t) \tag{14b}$$

Equations (11), (12*a*), (12*b*), (13), (14*a*), and (14*b*) are of importance. First, they drastically reduce the computational time since the results calculated for one mesh cycle can be easily extended to other periods by using matrix multiplication, which is computationally effective. Second, it allows an easier inversion of the matrix.

3.1 Response to Initial Conditions. Knowledge of the free response to initial conditions is important in assesing the dynamic stability property of the helical gear pair. Within each interval $t_{j-1} \leqslant t < t_j$, Eq. (9) can be rewritten in the homogeneous form as

$$\ddot{\delta}(t) + \left[a_j - 2q_j\left(-\frac{2t}{t_j - t_{j-1}} + 1 \right) \right] \delta(t) = 0,$$
$$t_{j-1} \leqslant t \leqslant t_j \quad (j = 1, \ldots, 6) \tag{15a}$$

$$\beta_j = \frac{1}{m_e}\left(\frac{K_j - K_{j-1}}{t_j - t_{j-1}} \right) \tag{15b}$$

$$\alpha_j = \frac{K_{j-1}}{m_e} - \beta_j t_{j-1} \tag{15c}$$

$$a_j = \alpha_j + \frac{\beta_j(t_j - t_{j-1})}{2} \tag{15d}$$

$$q_j = \frac{\beta_j(t_j - t_{j-1})}{4} \tag{15e}$$

With a change of variable $z_j=\alpha_j+\beta_j t$, Eqs. (15*a*)–(15*e*) are converted into the Stoke's equation [16] as

$$\frac{d^2\delta}{dz_j^2} + \frac{z_j}{\beta_j^2}\delta = 0 \tag{16}$$

A set of basis solutions are known over $t_{j-1} \leqslant t < t_j$

$$\gamma_1(t) = \sqrt{z_j}J_{1/3}(\sigma_j) \tag{17a}$$

$$\gamma_2(t) = \sqrt{z_j}J_{-1/3}(\sigma_j) \tag{17b}$$

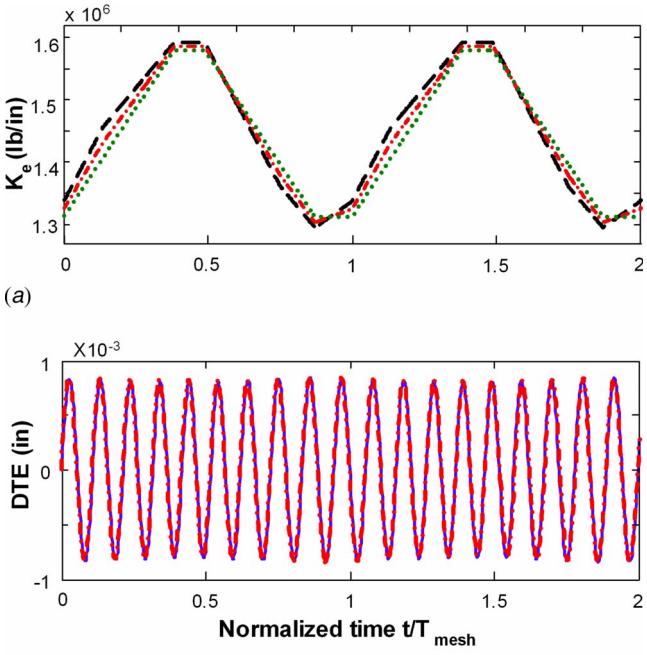

Fig. 5 (*a*) Effective stiffness. (*b*) homogeneous response predictions within two mesh cycles, given $x_0=2\times10^{-6}$ in. and $v_0=20$ in./s at $\Omega_p=1000$ rpm. Key: green dotted line, $\mu=0$; red dashed-dotted line, $\mu=0.2$; black dashed line, $\mu=0.4$ (analytical solution by the Floquet theory); blue solid line, $\mu=0.2$ (numerical solution).

where $\sigma_j=2z_j^{3/2}(3\beta_j)^{-1}$ and $J_{\pm1/3}(\sigma_j)$ are the Bessel functions of the first kind of order $\pm1/3$. We use the recurrence relation of Bessel functions to find the Wronskian matrix as

$$\Pi_j(t) = \begin{bmatrix} \sqrt{z_j}J_{1/3}(\sigma_j) & \sqrt{z_j}J_{-1/3}(\sigma_j) \\ z_jJ_{-2/3}(\sigma_j) & -z_jJ_{2/3}(\sigma_j) \end{bmatrix} \tag{18a}$$

$$\Pi_j^{-1}(t) = -\frac{2\pi}{3\sqrt{3}\beta_j}\begin{bmatrix} -z_jJ_{2/3}(\sigma_j) & -\sqrt{z_j}J_{-1/3}(\sigma_j) \\ -z_jJ_{-2/3}(\sigma_j) & \sqrt{z_j}J_{1/3}(\sigma_j) \end{bmatrix} \tag{18b}$$

Note that Eqs. (17*a*), (17*b*), (18*a*), and (18*b*) are valid only for the conditions with $z_j>0$. For cases in which z_j are negative (or zero), the Wronskian matrices are derived in terms of the modified Bessel functions of the first kind (or gamma functions), which could be treated in a similar matter. However, for the SDOF helical gear model with a high positive mean component, all z_j have positive values so that Eqs. (17*a*), (17*b*), (18*a*), and (18*b*) hold. Also, for intervals with a negative slope β_j (such as contact regions 4 and 5 of Fig. 4), the corresponding σ_j also has negative values, which lead to complex $\Pi_j(t)$ generated by the Bessel functions in Eqs. (17*a*), (17*b*), (18*a*), and (18*b*). Nevertheless, due to the supplemental phase relationship between $\Pi(t_j)$ and $\Pi^{-1}(t_{j-1})$, the state transition matrix $\Phi(t_{j-1},t_j)=\Pi(t_j)\Pi^{-1}(t_{j-1})$ still assumes real values within each interval $t_{j-1} \leqslant t < t_j$. Thus, responses to initial conditions $X(0)=\{\delta(0),\dot{\delta}(0)\}^T$ are derived in Eq. (19), where $\Phi(T,0)$ is the discrete transition matrix. Here, $\Phi(t-nT,0)$ needs to be evaluated, similar to Eq. (11) over the last cycle,

$$X(t) = \Phi(t-nT,0)\Phi(T,0)^nX(0) \quad (0 \leqslant t-nT < T) \tag{19}$$

Figure 5 compares the homogeneous responses given in initial conditions $x_0=2\times10^{-6}$ in. and $v_0=20$ in./s at $\Omega_p=1000$ rpm, as

predicted by using the Floquet theory and the numerical solution (based on the Runge–Kutta scheme [17]). Since the numerical solution completely overlaps with the Floquet theory prediction, only one pair of comparative results are given with $\mu=0.2$ in Fig. 5(*b*). Observe that increasing sliding friction changes the slopes of the effective stiffness function $K_{e,j}(t)$, while such effect does not seem to be significant for the DTE response. This is because the undamped responses are dictated by the dynamic components at the system natural frequency $f_n=\sqrt{\bar{K}_e}/(2\pi\sqrt{m_e})$, where $\bar{K}_e$ is the averaged stiffness. For the sample case, f_n is found to be close to $9.5f_m$, where f_m is the mesh frequency at $\Omega_p=1000$ rpm. Sidebands around $8.5f_m$ and $10.5f_m$ may also be present due to modulation effects.

The damped homogeneous response could also be derived by assuming $C_{e,i}(t)=2\zeta_e\sqrt{m_eK_e(t)}\approx 2\zeta_e\sqrt{m_e\bar{K}_e}=C_{e0}$ with a time-averaged viscous damping C_{e0}. Thus, Eqs. (7*a*)–(7*e*) is converted into the constantly damped homogeneous form as follows:

$$m_e\ddot{\delta}_d(t)+C_{e0}\dot{\delta}_d(t)+K_e(t)\delta_d(t)=0 \tag{20a}$$

By defining the transformation $\delta_d(t)=\psi(t)e^{-C_{e0}t/2}=\psi(t)e^{-\zeta_e\sqrt{\bar{K}_e}t/\sqrt{m_e}}$, Eq. (20*a*) is further converted into the following expression:

$$m_e\ddot{\psi}(t)+\left(1-\zeta_e^2\frac{\bar{K}_e}{K_e(t)}\right)K_e(t)\psi(t)=0 \tag{20b}$$

Since $\bar{K}_e/K_e(t)\approx 1$ for small viscous damping (say, $\zeta_e=5\%$), its square value (2.5×10^{-3}) is negligible compared with 1. Hence, Eq. (20*b*) assumes the same form as the undamped Eqs. (15*a*)–(15*e*), and it should have the same solution. This implies that for an oscillator with small viscous damping, the damped homogeneous response could be calculated as follows, where $\delta(t)$ is the analytical solution to the undamped system:

$$\delta_d(t)=\delta(t)e^{-\zeta_e\sqrt{\bar{K}_e/m_e}t} \tag{21}$$

Figure 6 shows that the analytical prediction of the damped homogeneous response with a constant $C_{e0}=2\zeta_e\sqrt{m_e\bar{K}_e}$ correlates well the numerical simulation with a time-varying $C_e(t)$ of Eq. (7*d*). Here, the $K_e(t)$ profile is the same as that illustrated in Fig. 5(*a*), with $\mu=0.2$. This implies that Eq. (21) could be used to approximate the homogeneous response with periodically varying stiffness and viscous damping parameters.

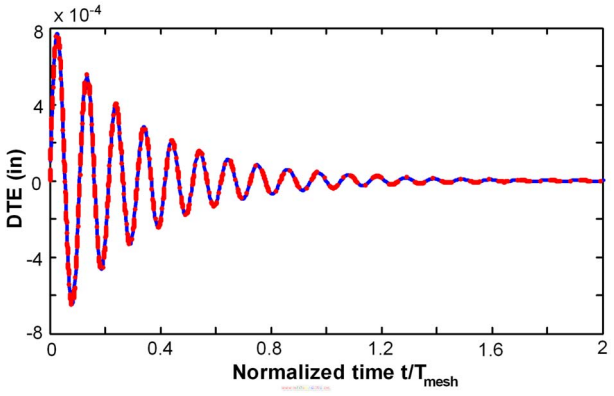

Fig. 6 Predictions of damped homogeneous responses within two mesh cycles, given $x_0=2\times10^{-6}$ in., $v_0=20$ in./s, and $\mu=0.2$ at $\Omega_p=1000$ rpm. Key: blue solid line, analytical solution by the Floquet theory with C_{e0}; red dashed-dotted line, numerical with $C_e(t)$.

3.2 Forced Periodic Response. For the LTV system of Eq. (9), Φ could be applied to compute the response under a periodic excitation. The tractability of the solution depends on both the characteristics of the excitation and the nature of Φ. In general, this problem is solved by expanding the forcing function as well as the time-varying parameters in terms of Fourier series. Clearly, this will lead to errors due to truncation of modes and also significantly increase the computations [6]. For the sample helical gear pair, three (or six) piecewise linear segments need to be considered for each mesh cycle without (or with) the influence of sliding friction. All integrals associated with the Floquet theory could be analytically found under a mean torque excitation. However, as the number of piecewise linear segments increases within the mesh cycle, such as for the realistic stiffness profile, analytical solutions could become computationally expensive. The forced response is formulated as follows:

$$X(t)=\Pi(t)\Pi^{-1}(t)X(0)+\int_0^t\Pi(t)\Pi^{-1}(\tau)F(\tau)d\tau \tag{22}$$

Since the initial condition response $\Pi(t)\Pi^{-1}(t)X(0)$ has already been derived in Eq. (19), only the forced response needs to be derived by applying $\Phi(t,0)=\Phi(t,\tau)\Phi(\tau,0)$ for any τ,

$$X(t)=\Phi(t,0)\left[\int_0^{nT}\Phi^{-1}(\tau,0)F(\tau)d\tau+\int_{nT}^t\Phi^{-1}(\tau,0)F(\tau)d\tau\right]$$
$$=\Phi(t,0)[H_1(n)+H_2(t)] \tag{23}$$

The solution is found in two parts, including the integral number of mesh cycles (H_1) and the last cycle (H_2) [6]. For n complete cycles, the expression for $H_1(t)$ is given as

$$H_1(n)=\sum_{i=1}^n\int_{(i-1)T}^{iT}\Phi_i^{-1}(\tau,0)F(\tau)d\tau \tag{24}$$

We define $\tau_0=\tau+(i-1)T$ and apply the Floquet theory such that

$$H_1(n)=\sum_{j=1}^n\left\{[\Phi^{-1}(T,0)]^{j-1}\left[\Pi_1(t_0)\int_0^{t_1}\Pi_1^{-1}(\tau)F(\tau_0)d\tau+\Pi_1(t_0)\Pi_1^{-1}(t_1)\Pi_2(t_1)\int_{t_1}^{t_2}\Pi_2^{-1}(\tau)F(\tau_0)d\tau\right.\right.$$
$$\left.\left.+\Pi_1(t_0)\Pi_1^{-1}(t_1)\Pi_2(t_1)\Pi_2^{-1}(t_2)\Pi_3(t_2)\int_{t_2}^{t_3}\Pi_3^{-1}(\tau)F(\tau_0)d\tau+\cdots\right]\right\} \tag{25}$$

For the last time cycle, the value of $H_2(t)$ depends on the time instant t in the whole mesh cycle. Hence, solutions are derived within each piecewise linear segment as follows, where $\tau_0=\tau+nT$,

$$H_2(t) = [\Phi^{-1}(T,0)]^n \left[\Pi_1(0) \int_0^{t-nT} \Pi_1^{-1}(\tau) F(\tau_0) d\tau \right]$$

$$= [\Phi^{-1}(T,0)]^n \times \begin{cases} \Pi_1(0) \displaystyle\int_{t_1}^{t-nT} \Pi_1^{-1}(\tau) F(\tau_0) d\tau & (t_0 \leqslant t - nT < t_1) \\ \left[\Pi_1(0) \displaystyle\int_0^{t_1} \Pi_1^{-1}(\tau) F(\tau_0) d\tau + \Pi_1(0) \Pi_1^{-1}(t_1) \Pi_2(t_1) \int_{t_1}^{t-nT} \Pi_2^{-1}(\tau) F(\tau_0) d\tau \right] & (t_1 \leqslant t - nT < t_2) \\ \cdots \\ \left[\Pi_1(0) \displaystyle\int_0^{T} \Pi_1^{-1}(\tau) F(\tau_0) d\tau + \cdots + \Pi_1(0) \Pi_1^{-1}(t_1) \Pi_2(t_1) \Pi_2^{-1} \cdots \Pi_j(t_{j-1}) \int_{t_{j-1}}^{t-nT} \Pi_j^{-1}(\tau) F(\tau_0) d\tau \right] & (t_{j-1} \leqslant t - nT < t_j,\ t_6 = T) \end{cases} \tag{26}$$

All matrices in Eq. (26) have been analytically derived, except for the $\int \Pi^{-1}(\tau) F(\tau) d\tau$ integral, which could be analytically found by using Eqs. (27*a*)–(27*h*), where Lommel*S*1 is the Lommel function [18]. Note that the constant forcing function $F(t) = \{0\ F_e/m_e\}^T$ could be taken out of the integral,

$$\int z J_{2/3}(\sigma) dt = -\sqrt{z} J_{-1/3}(\sigma) \tag{27a}$$

$$\int -\sqrt{z} J_{-1/3}(\sigma) dt = \frac{4\sigma}{3} J_{-1/3}(\sigma) L_1 + \sigma J_{-4/3}(\sigma) L_2 \tag{27b}$$

$$\int z J_{-2/3}(\sigma) dt = \sqrt{z} J_{1/3}(\sigma) \tag{27c}$$

$$\int \sqrt{z} J_{2/3}(\sigma) dt = -\frac{2\sigma}{3} J_{1/3}(\sigma) L_3 - \sigma J_{-2/3}(\sigma) L_4 \tag{27d}$$

$$L_1 = \text{Lommel}S1\left(-1, -\tfrac{4}{3}, \tfrac{2}{3}\beta z^{3/2}\right) \tag{27e}$$

$$L_2 = \text{Lommel}S1\left(0, -\tfrac{1}{3}, \tfrac{2}{3}\beta z^{3/2}\right) \tag{27f}$$

$$L_3 = \text{Lommel}S1\left(-1, -\tfrac{2}{3}, \tfrac{2}{3}\beta z^{3/2}\right) \tag{27g}$$

$$L_4 = \text{Lommel}S1\left(0, \tfrac{1}{3}, \tfrac{2}{3}\beta z^{3/2}\right) \tag{27h}$$

Analytical predictions of forced responses by using Eqs. (22)-(26), and (27*a*)–(27*h*) compare well with numerical results in Fig. 7, given $C_e(t)=0$, $x_0=2\times10^{-6}$ in., $v_0=20$ in./s, $T_p=2000$ lb in., $\mu=0.2$, and $\Omega_p=1000$ rmp. Here, the $K_e(t)$ profile is the same as in Fig. 5(*a*), with $\mu=0.2$; thus, six piecewise contact regions are considered within each mesh cycle. Similar to the undamped homogeneous response, the forced responses are also dominated by the dynamic component at the system natural frequency and some sidebands due to the modulation effect. Such resonances, however, are controlled by the viscous damping, which may have negligible effects on the mesh harmonics. Consequently, if the mesh harmonics do not coincide with the resonant frequency, one can approximate the damped dynamic responses by filtering out the resonant components from the undamped responses in frequency domain. For example, a low pass filter is used since $f_n \gg f_m$.

Analytical predictions of (undamped) forced responses are compared in Fig. 8 with numerical simulations obtained from a viscously damped SDOF model as well as a 6DOF model, which is similar to the 12DOF model in Ref. [1]. A comparison of steady-state time domain responses in Fig. 8(*a*) shows that the numerical simulation of the DTE predicted by the SDOF model matches well with that of the 6DOF model despite an offset in the mean component. Also, a viscous damping coefficient of 5% tends to "remove" the dominant resonant components (as compared to the mesh harmonics) from the undamped forced response. Next, the steady-state time responses are converted into frequency domain, and Fig. 8(*b*) (where the static term is cut off) shows that predictions at the first five mesh harmonics of the undamped system match very well with the spectra of viscously damped responses calculated by numerical integration. This suggests that the analytical solution could be extended to examine the damped dynamic response in frequency domain.

Figure 9(*a*) shows the predicted mesh harmonics of DTE as a function of μ. Observe that an increase in μ has the most significant effect on the first two mesh harmonics. Figure 9(*b*) shows the derivatives of DTE harmonics with respect to μ; these are approximated by the finite difference method, i.e., $d\delta/d\mu \approx [\delta(n) - \delta(n-1)]/[\mu(n) - \mu(n-1)]$. Observe that the second harmonic has the highest increasing rate, followed by the first harmonic. Moreover, since the amplitude at the second harmonic without friction ($\mu=0$) is much smaller than that of the first harmonic, it is

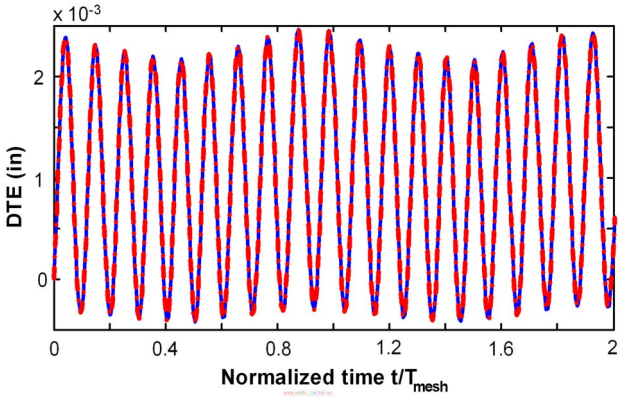

Fig. 7 Predictions of (undamped) forced periodic responses within two mesh cycles, given $x_0=2\times10^{-6}$ in., $v_0=20$ in./s, $T_p=2000$ lb in., and $\mu=0.2$ at $\Omega_p=1000$ rpm. Key: blue solid line, analytical solution by the Floquet theory; red dashed-dotted line, numerical solution.

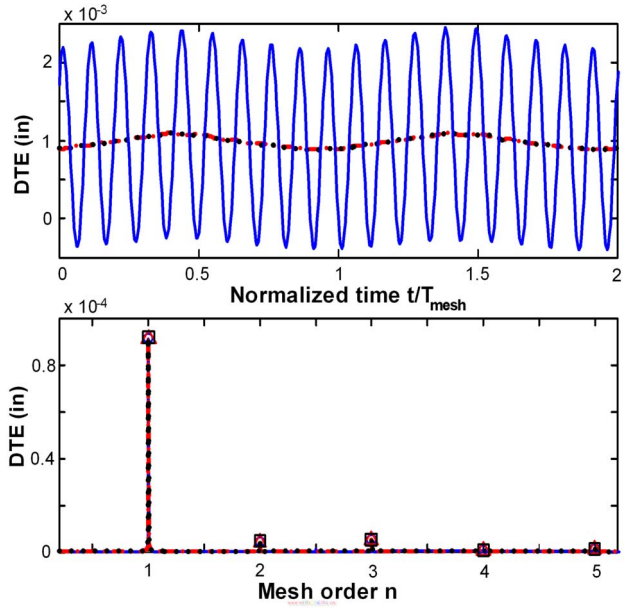

Fig. 8 Steady-state forced periodic responses given $x_0=2\times10^{-6}$ in., $v_0=20$ in./s, $T_p=2000$ lb in., and $\mu=0.1$ at $\Omega_p=1000$ rpm: (*a*) DTE versus time; (*b*) DTE spectra. Key: blue solid line with ○, undamped analytical prediction; black dotted line with □, damped numerical simulation of the SDOF system with $\zeta_e=5\%$; red dashed-dotted line with △, damped numerical simulation of a 6DOF model with $\zeta_e=5\%$ (with mean component compensated).

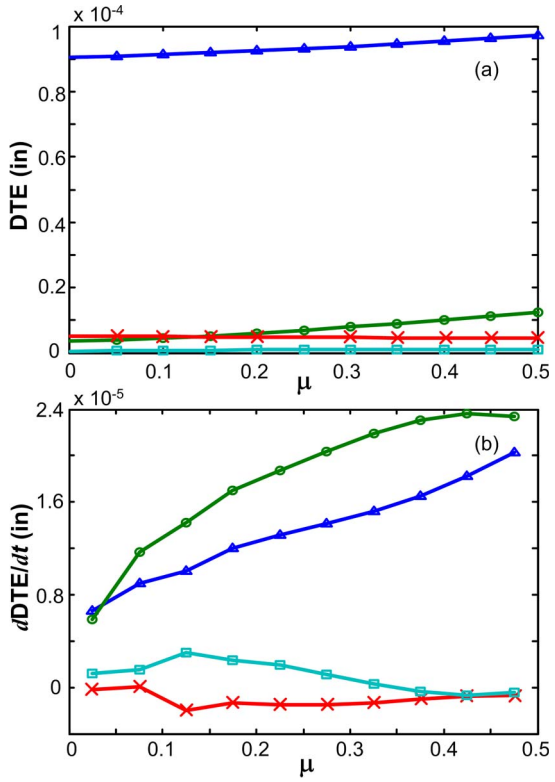

Fig. 9 Predicted mesh harmonics of (undamped) forced periodic responses as a function of μ, given $x_0=2\times10^{-6}$ in., $v_0=20$ in./s, and $T_p=2000$ lb in. at $\Omega_p=1000$ rpm: (*a*) DTE; (*b*) slope of DTE. Key: blue line with △, $n=1$; green line with ○, $n=2$; red line with ×, $n=3$; and cyan line with □, $n=4$.

implied that sliding friction has more influences on the second harmonic. This is consistent with the results predicted by the 12DOF formulation [1].

4 Conclusion

This paper extends the earlier work of Vaishya and Singh [6] by applying the Floquet theory to a helical gear pair to examine the effect of sliding friction on the DTE. In particular, the LTV formulations (with parametric excitations) have been developed for a SDOF model, and the effect of sliding friction is quantified as parametric excitations of effective mesh stiffness. The Floquet theory has been successfully applied to obtain closed-form DTE solutions, given periodic and piecewise linear stiffness functions. Responses to both initial conditions and forced periodic functions, under a nominal preload, are derived. Analytical models have been validated by comparing predictions with numerical simulations. Although the coefficient of friction μ is assumed to be high for the sample case for illustrative purposes, the same algorithm could be implemented under realistic conditions when a smaller value of μ is expected. Overall, the sliding friction has a marginal effect on the DTE of helical gears, as compared with spur gears [8], at least in the context of the torsional model. Finally, parametric instability issues are briefly examined as follows. Asymptotic stability of a homogeneous system can be determined from the discrete transition matrix Φ over one complete period of parametric changes [6]. A sufficient condition for stability is that all the eigenvalues κ of the $\Phi(T,0)$ matrix have absolute values less than unity [16]. For the sake of illustration, Fig. 10 shows the mapping of maximum κ (absolute value) as a function of the ratio of time-varying mesh frequency $f_m(t)$ to the system natural frequency f_n, without viscous damping. Observe that the most dominant unstable region emerges when $f_m(t)/f_n \approx 2$; such parametric instability is well explained by Den Hartog [19]. Other unstable regions are found when the ratio of $f_m(t)/f_n$ is close to 1, 2/3, 1/3, etc. Also, an increase in μ tends to enhance the $\max\{|\kappa|\}$ value in the most dominant unstable region around $f_m(t)/f_n \approx 2$; in addition, it decreases the 1/3 peak while enhancing the peak around 1. When the system operates near unstable regions, various stability performances could be observed though these results are not shown here. For instance, when $f_m(t)/f_n$ is close to 2 (say, at 18,000 rpm), long term stability performance is observed. On the other hand, when $f_m(t)/f_n$ falls within the unstable region (say, at 19,000 rpm), the homogeneous response grows unbounded.

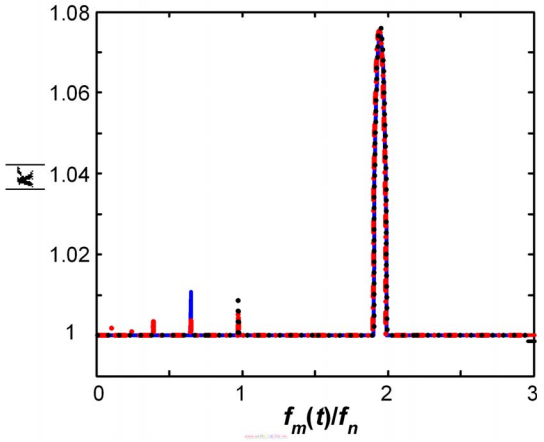

Fig. 10 Mapping of eigenvalue κ (absolute value) maxima as a function of the ratio of time-varying mesh frequency $f_m(t)$ to the system natural frequency f_n. Key: —, $\mu=0.01$; ---, $\mu=0.1$; and ⋯, $\mu=0.2$.

Acknowledgment

We acknowledge Prof. G. Pavic (INSA Lyon, France) for supporting the first author (in early 2007) and Dr. T. Rook (Goodrich Co.) for his valuable suggestions.

References

[1] He, S., Gunda, R., and Singh, R., 2007, "Inclusion of Sliding Friction in Contact Dynamics Model for Helical Gears," ASME J. Mech. Des., **129**, pp. 48–57.
[2] Velex, P., and Cahouet, V., 2000, "Experimental and Numerical Investigations on the Influence of Tooth Friction in Spur and Helical Gear Dynamics," ASME J. Mech. Des., **122**(4), pp. 515–522.
[3] Velex, P., and Sainsot, P., 2002, "An Analytical Study of Tooth Friction Excitations in Spur and Helical Gears," Mech. Mach. Theory, **37**, pp. 641–658.
[4] Lundvall, O., Strömberg, N., and Klarbring, A., 2004, "A Flexible Multi-Body Approach for Frictional Contact in Spur Gears," J. Sound Vib., **278**(3), pp. 479–499.
[5] Vaishya, M., and Singh, R., 2003, "Strategies for Modeling Friction in Gear Dynamics," ASME J. Mech. Des., **125**, pp. 383–393.
[6] Vaishya, M., and Singh, R., 2001, "Analysis of Periodically Varying Gear Mesh Systems With Coulomb Friction Using Floquet Theory," J. Sound Vib., **243**(3), pp. 525–545.
[7] Vaishya, M., and Singh, R., 2001, "Sliding Friction-Induced Non-Linearity and Parametric Effects in Gear Dynamics," J. Sound Vib., **248**(4), pp. 671–694.
[8] He, S., Gunda, R., and Singh, R., 2007, "Effect of Sliding Friction on the Dynamics of Spur Gear Pair With Realistic Time-Varying Stiffness," J. Sound Vib., **301**, pp. 927–949.
[9] Borner, J., and Houser, D. R., 1996, "Friction and Bending Moments as Gear Noise Excitations," SAE Trans., **105**(6), pp. 1669–1676.
[10] Padmanabhan, C., Barlow, R. C., Rook, T. E., and Singh, R., 1995, "Computational Issues Associated With Gear Rattle Analysis," ASME J. Mech. Des., **117**, pp. 185–192.
[11] Xiao, D. Z., Gao, Y., Wang, Z. Q., and Liu, D. M., 2005, "Conjugation Criterion for Making Clearance of the Meshed Helical Surfaces," ASME J. Mech. Des., **127**(1), pp. 164–168.
[12] 2003, Helical3D (CALYX software), "Helical3D User's Manual," ANSOL Inc., Hilliard, OH (www.ansol.www).
[13] Tamminana, V. K., Kahraman, A., and Vijayakar, S., 2007, "A Study of the Relationship Between the Dynamic Factors and the Dynamic Transmission Error of Spur Gear Pairs," ASME J. Mech. Des., **129**(1), pp. 75–84.
[14] Abousleiman, V., Velex, P., and Becquerelle, S., 2007, "Modeling of Spur and Helical Gear Planetary Drives With Flexible Ring Gears and Planet Carriers," ASME J. Mech. Des., **129**(1), pp. 95–106.
[15] Guilbault, R., Gosselin, C., and Cloutier, L., 2005, "Express Model for Load Sharing and Stress Analysis in Helical Gears," ASME J. Mech. Des., **127**(6), pp. 1161–1172.
[16] Richards, J. A., 1983, *Analysis of Periodically Time-Varying Systems*, Springer, New York.
[17] Cartwright, J. H. E., and Piro, O., 1992, "The Dynamics of Runge-Kutta Methods," Int. J. Bifurcation Chaos Appl. Sci. Eng., **2**, pp. 427–449.
[18] Gray, A., and Mathews, G. B., 1966, *A Treatise on Bessel Functions and Their Applications to Physics*, Dover, New York.
[19] Den Hartog, J. P., 1956, *Mechanical Vibrations*, Dover, New York.